Applied Computing and Geosciences 9 (2021) 100051

Contents lists available at ScienceDirect

Applied Computing and Geosciences

journal homepage: www.journals.elsevier.com/applied-computing-and-geosciences

Retrieval of land surface temperature, normalized difference moisture index, normalized difference water index of the Ravi basin using Landsat data

Ajay Kumar Taloor [a,*], Drinder Singh Manhas [a], Girish Chandra Kothyari [b]

[a] Department of Remote Sensing and GIS, University of Jammu, Jammu, 180 006, India
[b] Institute of Seismological Research Gandhinagar, Gujarat, India

ARTICLE INFO

Keywords:
Land surface temperature (LST)
Normalized difference vegetation index (NDVI)
Normalized difference moisture index (NDMI)
Normalized difference water index (NDWI)

ABSTRACT

Land surface temperature (LST) is an important parameter for the biosphere, cryosphere, and climate change studies. In this study, we estimate LST, NDMI, and NDWI over the Ravi basin, India, and parts of Pakistan, using Landsat-8 Operational Land Imager (OLI) and Thermal Infrared Sensor (TIRS) data. The study develops an ERDAS IMAGINE image processing method by using the LANDSAT 8 band 3(Green), band 4(Red), band 5(NIR), band 6(SWIR 1), and band 10 (TIR) data for determining the various spectral indices. The LST results show that most of the areas experienced extreme anomalies ranging from -35^{0}Cand 36 °C. The normalized difference moisture index (NDMI) value ranges from 0.685 to - 0.154. The normalized difference water index (NDWI) value ranges from 0.146 to - 0.444. Further, the LST result validated with *in situ* temperature observations at six locations in the study area, providing excellent correlation.

1. Introduction

Remote Sensing (RS) and Geographic Information Systems (GIS) have enhanced man's capability to look at the world with sensors to observe the dynamic changes on the Earth's surface. This revolution has made it quite easy for the human beings to determine changes spatially as well as temporally over a larger area. Among the various application in geoscience and natural resources management, the environmental and climatological aspects are particularly well understood by RS and GIS (Alam et al., 2017, 2018; Kannaujiya et al., 2020; Kothyari et al., 2019; Sarkar et al., 2020b; Sharma et al., 2020; Taloor et al., 2017, 2019, 2020a, 2020b). The LST is represents the temperature of the Earth's surface, and also a temperature at the interface between the Earth's surface and its atmosphere (Lejeune et al., 2015; Malik and Shukla, 2018; Niclòs et al., 2009; Singh et al., 2020; Sood et al., 2020a). Moreover, there is a sense of curiosity and growing awareness about climate change due to rising temperatures over the years. This has led geospatial scientists to realize that remote sensing must play an important role in providing data needed to assess ecosystems conditions and to monitor change at all spatial and temporal scales (Singh et al., 2017; Sarkar et al., 2020a; Taloor et al., 2020c; Kothyari et al., 2020a; 2020b; 2020c).

Since 1978 there has been a continuous day and night coverage of the thermal data at 4 km resolution and selective coverage at greater resolutions such as with the Geostationary Operational Environmental Satellite (GOES), NOAA-Advanced Very High Resolution Radiometer (AVHRR), and Terra and Aqua- Moderate Resolution Imaging Spectroradiometer (MODIS). The heat capacity mapping mission (HCMM), which was specially designed for the measurement of thermal inertia and thermal discrimination of various surface materials (Drury, 1987), is among the few developed before the 1980s. With the enhancement of technology, high resolution data from the new sensors is available: e.g. the Terra-Advanced Space borne Thermal Emission and Reflection Radiometer (ASTER) has a 90 m resolution and Landsat-7 Enhanced Thematic Mapper (ETM+) and Landsat-8 TIRS have a resolution of 100 m in the thermal region. Sentinel −3 gridded land surface temperature, generated on a wide 1 km measurement grid, is among the new data with a wider application to LST estimation (Barsi et al., 2014; Guha et al., 2020a).

Due to the limitations of in-situ observations of surface temperature globally, satellite based LST provides relatively large spatial variability, high resolution, and consistent and repetitive coverage of measurements of earth surface conditions on a regional or global basis (Owen et al., 1998; Malik and Shukla; 2018; Guhan et al., 2020; Yan et al., 2020). Over the years satellite based LST has become an important parameter for

* Corresponding author.
E-mail address: ajaytaloor@gmail.com (A.K. Taloor).

https://doi.org/10.1016/j.acags.2020.100051
Received 12 August 2020; Received in revised form 22 December 2020; Accepted 22 December 2020
Available online 29 December 2020
2590-1974/© 2020 Published by Elsevier Ltd. This is an open access article under the CC BY-NC-ND license (http://creativecommons.org/licenses/by-nc-nd/4.0/).

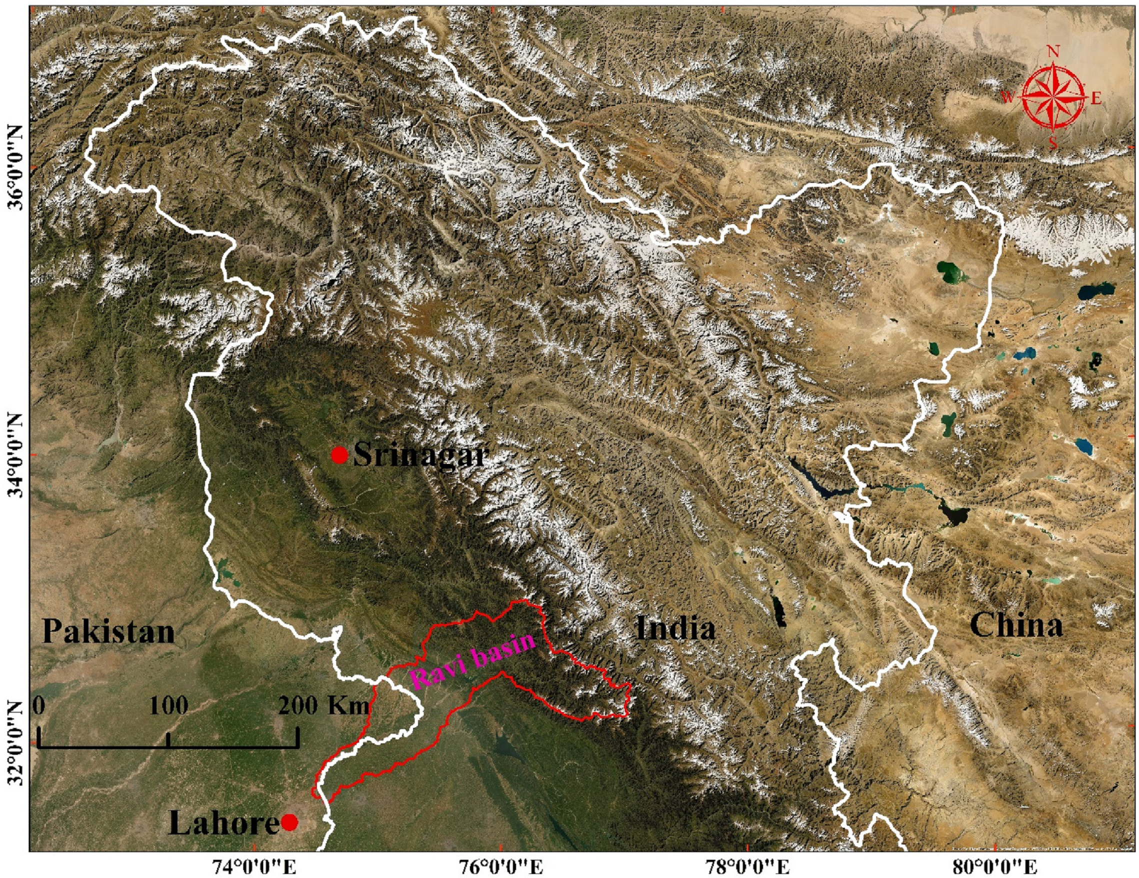

Fig. 1. Google map image location map of the study area.

studying agriculture processes, evapotranspiration, climate change, the hydrological cycle, forest fires, sensible and latent heat indices, vegetation monitoring, urban climate, urban heat islands and volcanic studies (Mannstein, 1987; Sellers et al., 1988; Bastiaanssen et al., 1998; Kogan, 2001; Su, 2002; Arnfield, 2003; Voogt and Oke, 2003; Weng et al., 2004; Kalma et al., 2008; Weng, 2009; van Leeuwen et al., 2011; Kour et al., 2016; Wanderley et al., 2019; Kumar et al., 2020; Sekertekin and Bonafoni, 2020).

Recent studies suggest the integration of multispectral bands with the TIR bands of Landsat images (TM, ETM+, OLI, and TIRS) has enhanced the ability of RS techniques to derive LST. Many techniques have been developed to estimate LST for various purposes, such as land surface emissivity (Reddy and Manikiam, 2017), urban heat analysis (Guo et al., 2015; Guhan et al., 2020), meteorology and climatology (Tomlinson et al., 2011; Sobrino and Raissouni, 2000), land use land cover (LULC) monitoring (Joshi and Bhat, 2012; Ahmad et al., 2013; Yao et al., 2018; Sahana et al., 2019; Gohian et al., 2020; Guha et al., 2020a), split window and single channel (Du et al., 2015; Hulley et al., 2014; Yu et al., 2014; Julien and Sobrino, 2009; Jiménez-Muñoz et al., 2008), the relationship between LST and NDWI (Guha et al., 2020a), and the normalized difference built-up index (NDBI) and LST (Chen et al., 2006; Yuan et al., 2017; Mustafa et al., 2020; Guha et al., 2020b).

Apart from LST estimation, the TIR region of the electromagnetic spectrum has huge potential to estimate land surface related changes in any region, and is abundantly applied in almost every sector of Earth science (Wen, 2017; Alexander, 2020; Khan et al., 2020). It has the potential to map more indices, which can easily provide a quick estimation. The NDWI is the most appropriate for water body mapping as a water body has strong absorbability and low radiation in the range from visible to infrared wavelength (McFeeters, 1996; Haque et al., 2020; Sarkar et al., 2020; Sood et al., 2020b). The NDMI, describes a crop's water stress level (Gao, 1996) and is calculated as the ratio between the difference and the sum of the refracted radiations in the near infrared and SWIR, that is as (NIR-SWIR)/(NIR + SWIR). The NDVI provides an estimation of the health of vegetation (Kriegler et al., 1969).

In the present study the estimation of the LST has been made from Landsat 8 using TIRS bands 10 and 11 in the Ravi basin, which highlight the highly heterogeneous characteristics of the land surface. The normalized difference vegetation index (NDVI) has also been calculated to draw out the vegetation index effect on LST in the area. Similarly, NDMI was also calculated for determining the water index effect on LST.

2. Description of study area

The Ravi River basin extends from 74°20′ E to 77°02′ E longitude and from 31°31′ N to 33°02′ N latitude in the Himachal Pradesh (HP), Jammu and Kashmir (JK), and Punjab(PB) states of India and some parts of Pakistan, covering a total area of 12702 km^2, with a flowing length of 720 km in India (Fig. 1). Being a transboundary river crossing northwestern India and eastern Pakistan, it is one of the six major rivers of the Indus basin and as per the Indus Water Treaty (IWT) of 1960 (IWT, 1960) the water of this river is allocated to India. The river rises in the Raigarh Glacier (snout ~4050 m above mean sea level (amsl) in the Bara Bhangal region of the Pir-Panjal range in the state of Himachal Pradesh. The study area has a mountainous hilly area in its northern parts with large numbers of glaciers, lush green fields, mountain valleys and tracts of Indo Gangetic plains in its southern parts covering the state of Punjab in India. The Ravi and Ujh are the two major rivers of the study area flowing in a southwest direction (Fig. 2). The Indian summer monsoon (ISM), during the months of April to September, generally accounts for 55% of the total annual rainfall, while mid-latitude westerlies, which is also called the Indian winter monsoon (IWM), from November to March contribute 35%

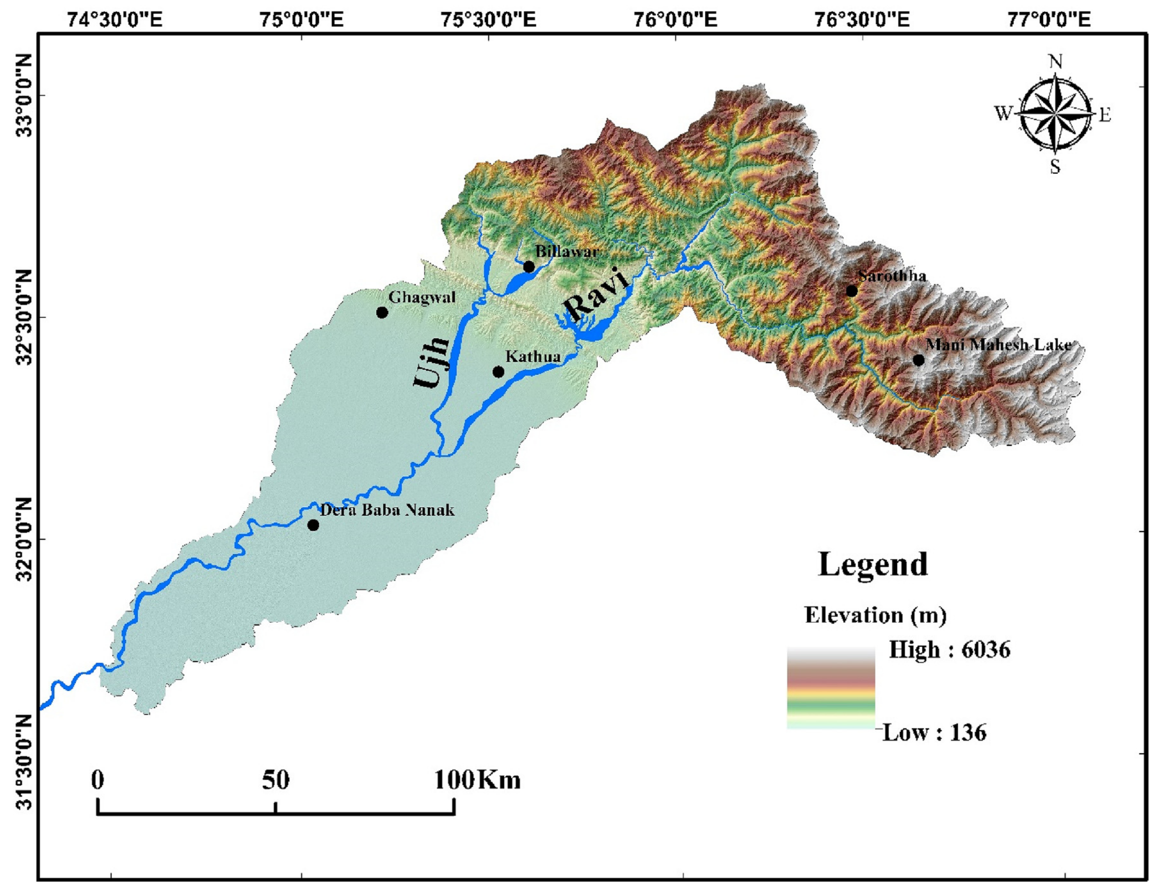

Fig. 2. Shuttle Radar Topography Mission (SRTM), derived digital elevation model (DEM) with 30 m resolution, and shaded relief elevation map of the Ravi basin overlain by the Ravi and Ujh rivers.

(Pareta and Pareta, 2014; Chand and Sharma, 2015). The structurally controlled hydrology of the Ravi basin is mainly regulated by spring snowmelt and the summer monsoon rainfall (HPSEB, 2004; Chand and Sharma, 2015; Chand et al., 2019).

2.1. Land use/land cover map

LULC is one of the most important thematic layers to help understand the basic natural characteristics of any land surface. In the present study, identified LULC features are readily interpretable from the Landsat-8 data imagery. The identified classes (Fig. 3) are agriculture land covering the southern and some northern hilly tracts and account for 5806.90 km^2 (45.72%). The built-up area is shown in the false color composite(FCC) with a blocky appearance and light bluish colour, and is intermingled with the agriculture land and some major hilly towns of the state of HP, covering in total 542.87 km^2(4.27%) of the study area. The canal area covers 13.37 km^2 and (0.11%) of the total area. These canals are not used for irrigation purposes in study area but are further channelled into the arid state of Rajasthan for domestic and irrigation purposes. The fallow land mostly occurs along the Ravi river bed and also along the canals and covers 46.63 km^2(0.37%) of the study area, whereas the forest cover ranges from reddish, bright red to light grey colour in the FCC and accounts for a large chunk of the study area covering 3422.26 km^2 (26.94%). The snow cover in the north and northeast of the study area is shown in white colour in the FCC and accounts for 2503.40 (19.71%) of the study area. The rivers (Ravi and Ujh) account for 326.40 km^2 (2.57%) of the study area and appear as light blue to cyan colour. The vegetation covers 18.60 km^2 (0.15%) and includes orchards, social forestry and plantations in the plains of the state of PB, whereas the wasteland found along the India-Pakistan border accounts for 21.57 km^2 (0.17%) of the study area.

3. Data and methodology

In the present study, LANDSAT 8 data was used to determine the various indices by using the OLI and the TIR sensors. The OLI sensor provides data at a 30 m spatial resolution with eight bands located in the visible, near-infrared and the shortwave infrared regions of the electromagnetic spectrum, and with an additional panchromatic band of 15 m resolution. The TIRS senses the Thermal Infrared (TIR) radiance at a spatial resolution of 100 m using two bands located in the atmospheric window between 10 and 12 μm. The band designations of Landsat 8 are given in Table 1. To determine the results, the multispectral RS images of the Ravi basin from different dates were obtained from the United States Geological Survey (USGS). As one scene cannot cover the full study area, a total of five satellite images of Landsat 8 were used having different paths and rows (Table 2). All the satellite data are re-projected to a Universal Transverse Mercator (UTM) coordinate system, (datum WGS84, zone44). The algorithm was created in the ERDAS IMAGINE 2015 software, which is optimized to process the complexity Landsat-8 data. Landsat-8, band-10 was used to derive the LST, band 4 and 5 were used to calculate the NDVI, band 5 and 6 for were used for NDMI, and band 3 and 5 were used for the estimation of the NDWI. The methodology adopted in the present study is given in Fig. 4.

3.1. Conversion of DN values to at-sensor spectral radiance

The satellite data products were a geometrically corrected data set. The required metadata of the satellite images is presented in Table 3.

The first step of the proposed work is to convert the Digital Number

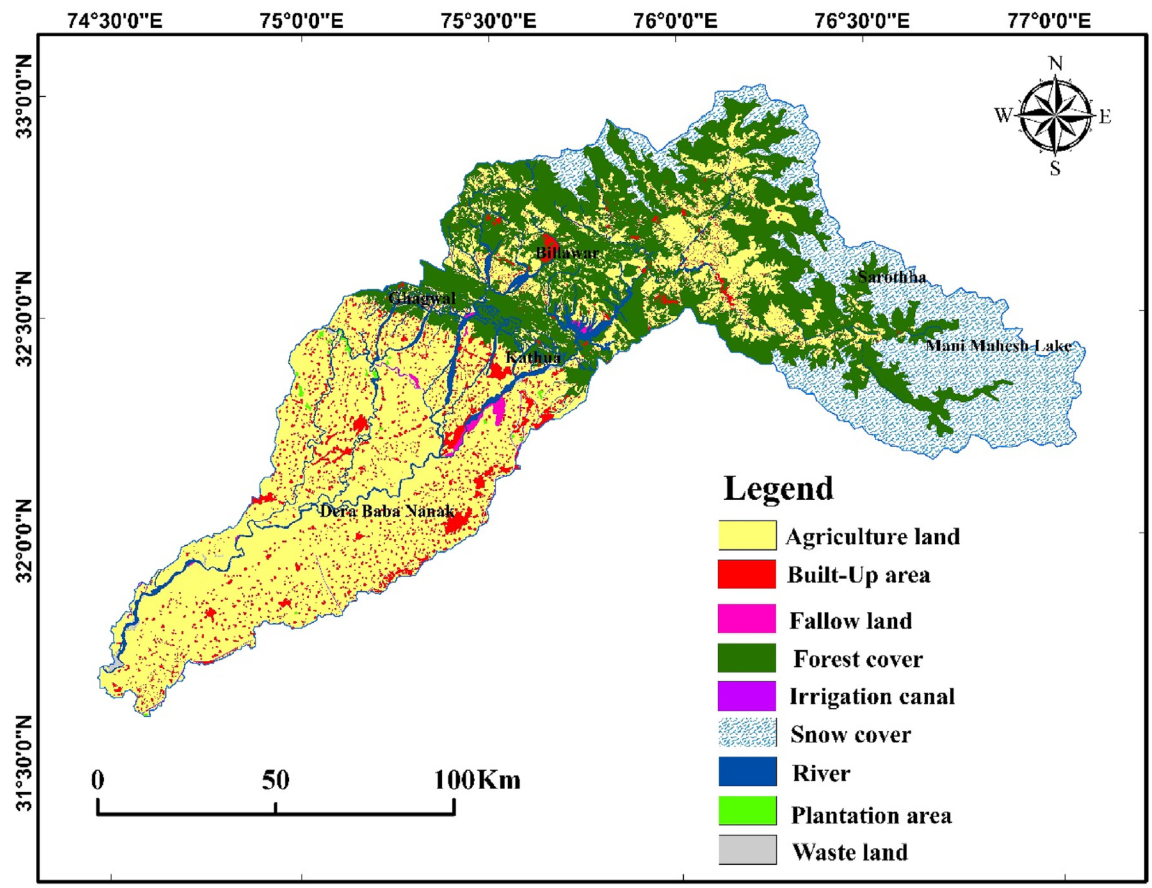

Fig. 3. Land use/land cover map of the study area.

Table 1
Landsat 8 OLI and TIRS sensor descriptions.

Band Designations	Wavelength (μm)	Resolution (m)
Band 1 (Coastal Aerosol)	0.43–0.45	30
Band 2 (Blue)	0.45–0.51	30
Band 3 (Green)	0.53–0.59	30
Band 4 (Red)	0.64–0.67	30
Band 5 (Infrared)	0.85–0.88	30
Band 6 (Short wave infrared)	1.57–1.65	30
Band 7 (Short wave infrared)	2.11–2.29	30
Band 8 (Panchromatic)	0.50–0.68	15
Band 9 (Cirrus)	1.36–1.39	30
Band 10 (Thermal infrared)	10.6–11.19	100
Band 11 (Thermal infrared)	11.50–12.51	100

(DN) values of band 10 to at-sensor spectral radiance using equation (1):

$$L_\lambda = \frac{(L_{max} - L_{min})^* Q_{cal}}{Q_{calmax} - Q_{calmix}} + L_{min} - O_i \quad (1)$$

where:

L_{max} is the maximum radiance ($Wm^{-2}sr^{-1}\mu m^{-1}$),
L_{min} is the minimum radiance ($Wm^{-2}sr^{-1}\mu\ m^{-1}$),
Q_{cal} is the DN value of pixel, $Q_{cal\ max}$ is the maximum DN value of pixels,
$Q_{cal\ min}$ is the minimum DN value of pixels, and
O_i is the correction value for band 10.

3.2. Conversion of DN to at-sensor spectral radiance

After converting DN values to at-sensor spectral radiance, the TIRS band data are converted to Brightness Temperature (BT) using equation (2), and the thermal constants given in Table 3.

$$BT = \frac{K2}{\ln\left[\left(\frac{K1}{L\lambda}\right) + 1\right]} - 273.15 \quad (2)$$

Table 2
Landsat data used.

S.No.		Data	Date	Path/Row	Band		
					For LST	For NDMI	For NDWI
1	Sarothha (HP)	LC08_L1TP_147037_20180211_20180222_01_T1	11-02-2018	47/37	TIRS1 & TIRS2	NIR & SWIR1	Green & Red
2	Mani Mahesh Lake (HP)	LC08_L1TP_147038_20180126_20180207_01_T1	26-01-2018	47/38	TIRS1 & TIRS2	NIR & SWIR1	Green & Red
3	Billawar	LC08_L1TP_148037_20180202_20180220_01_T1	02-02-2018	48/37	TIRS1 & TIRS2	NIR & SWIR1	Green & Red
4	Kathua	LC08_L1TP_148038_20180218_20180307_01_T1	18-02-2018	48/38	TIRS1 & TIRS2	NIR & SWIR1	Green & Red
5	Gaghwal	LC08_L1TP_149037_20180124_20180206_01_T1	24-01-2018	49/37	TIRS1 & TIRS2	NIR & SWIR1	Green & Red
6	Dera Baba Nanak	LC08_L1TP_149038_20180225_20180308_01_T1	25-02-2018	49/38	TIRS1 & TIRS2	NIR & SWIR1	Green & Red

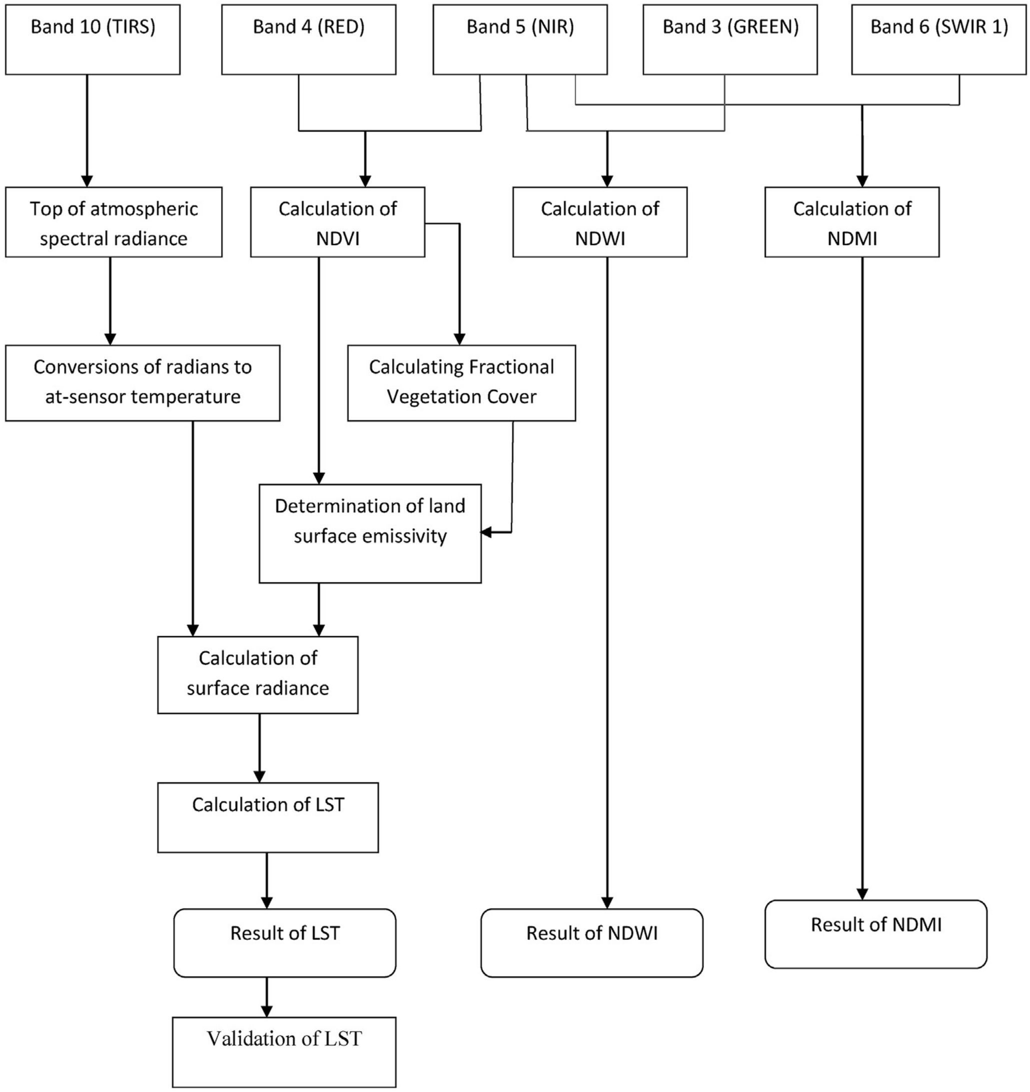

Fig. 4. Flow diagram showing methodology.

Table 3
Metadata of the satellite image.

Variable	Description	Value
K1	Thermal constants, band 10	774.8853
K2		1321.0789
L_{max}	Maximum and Minimum values of Radiance, Band 10	22.00180
L_{min}		0.10033
Q_{calmax}	Maximum and Minimum values of Quantize Calibration,	65535
Q_{calmin}	Band 10	1
O_i	Correction value, Band 10	0.29

where K1 and K2 are the thermal constants of TIR band 10, and can be identified in the metadata file associated with the satellite image. To have the results in degree Celsius, it is necessary to revise by adding absolute zero, which is approximately equal to −273.15 °C. Since the atmosphere in our research area is comparatively dry and therefore, the range of water vapor values is relatively small, the atmospheric effect is not taken into consideration in retrieving the LST.

3.3. Derivation of normalized difference vegetation index (NDVI)

The NDVI is essential to identify different land cover types in the study area and it ranges from −1.0 to +1.0 (Kriegler et al., 1969). The NDVI is calculated on a per-pixel basis as the normalized difference between the red band (0.64–0.67 μm) and near infrared band (0.85–0.88 μm) using the formula in equation (3).

$$NDVI = \frac{NIR - RED}{NIR + RED} \tag{3}$$

The calculation of NDVI is necessary to further calculate proportional vegetation (Pv) and emissivity () for the estimation of LST.

3.4. Estimation of fractional vegetation cover (FVC)

The FVC is generally defined as the ratio of the vertical projection area of vegetation (including leaves, stalks, and branches) on the ground to the total vegetation area. It is an important biophysical parameter for simulating the exchange between the land surface and the atmospheric boundary level using the soil-vegetation atmosphere transfer model (Liang et al., 2012). In the present study, we have used the remote sensing based approach to retrieve the FVC value.

FVC can be calculated using equation (4):

$$FVC = [(NDVI - NDVI_{min})/(NDVI_{max} - NDVI_{min})]^2 \tag{4}$$

where:

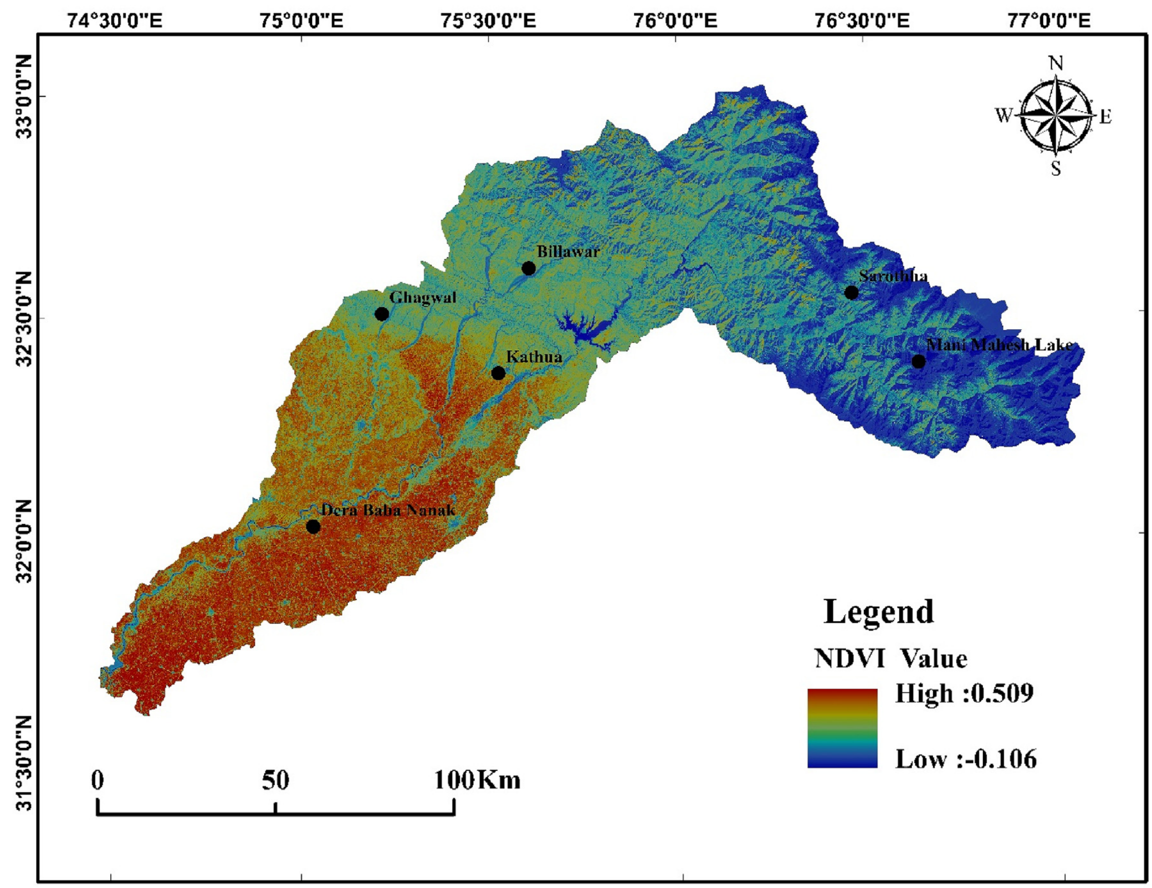

Fig. 5. NDVI map of the study area.

NDVI = DN values from NDVI Image,
$NDVI_{min}$ = Minimum DN values from NDVI Image,
$NDVI_{max}$ = Maximum DN values from NDVI Image.

3.5. *Estimation of land surface emissivity (LSE)*

The calculation of LSE is required to estimate LST.

The LSE is defined as the ratio of the radiance emitted by an object to the radiance it would emit if it were a perfect black body at the same thermodynamic temperature (Norman and Backer, 1995). Extensive measurements of LSE have been made because of its importance to satellite remote sensing of LST (Becker, 1987), surface energy balance estimation (Hall et al., 1992), mineral exploration, and identification and radiation budget calculation (Prata et al., 1997). The satellite based measurements can be modified by LSE in three ways:

- LSE reduces the top of atmosphere (ToA) radiances in comparison with a blackbody,
- Non-black body surfaces reflecting down welling radiances, and
- When we introduce the anisotropy of LSE, it reduces or increases surface leaving radiances.

LSE can be calculated using equation (5):

$$LSE = \varepsilon s \times (1\text{- } FVC) + (\varepsilon v \times FVC) \tag{5}$$

where:

εs = Emissivity of bare soil, εv = Emissivity of vegetation.

3. *6: calculation of surface radiance*

The surface temperature of the SCA (snow covered area) sunlit and SCA shadow is determined using the TIRS band 10 data of Landsat-8, centered at 10.9 μm. Relative to band 10, band 11 data (centered at 12 μm) is found to be affected by a larger stray light effect in the telescope, resulting in uncertainty in its calibration that restricts its further use (Barsi et al., 2014). To retrieve the surface temperature (Ts), initially the spectral radiance at the sensor is converted to the surface radiance, and then finally Ts is calculated using the surface radiance values as per equation (6).

$$LS = (Lsat – Lu) / \varepsilon\tau \text{ - } (1 \text{ - } \varepsilon) / \varepsilon \; Ld \tag{6}$$

where: LS = Surface radiance after atmospheric correction.

Lsat = Spectral radiance at the sensor,
Lu = Upwelling spectral radiance between the surface and the sensor,
ε = Emissivity,
τ = Atmospheric transmission, and
Ld = Downwelling spectral radiance from the sky.

3.7. *Calculation of land surface temperature (LST)*

The corrected surface radiance values of band 10 are converted into surface temperature using equation (7):

$$LTS = \frac{K2}{\mathrm{In}\left(\frac{K1}{LS}\right) + 1} \tag{7}$$

where:

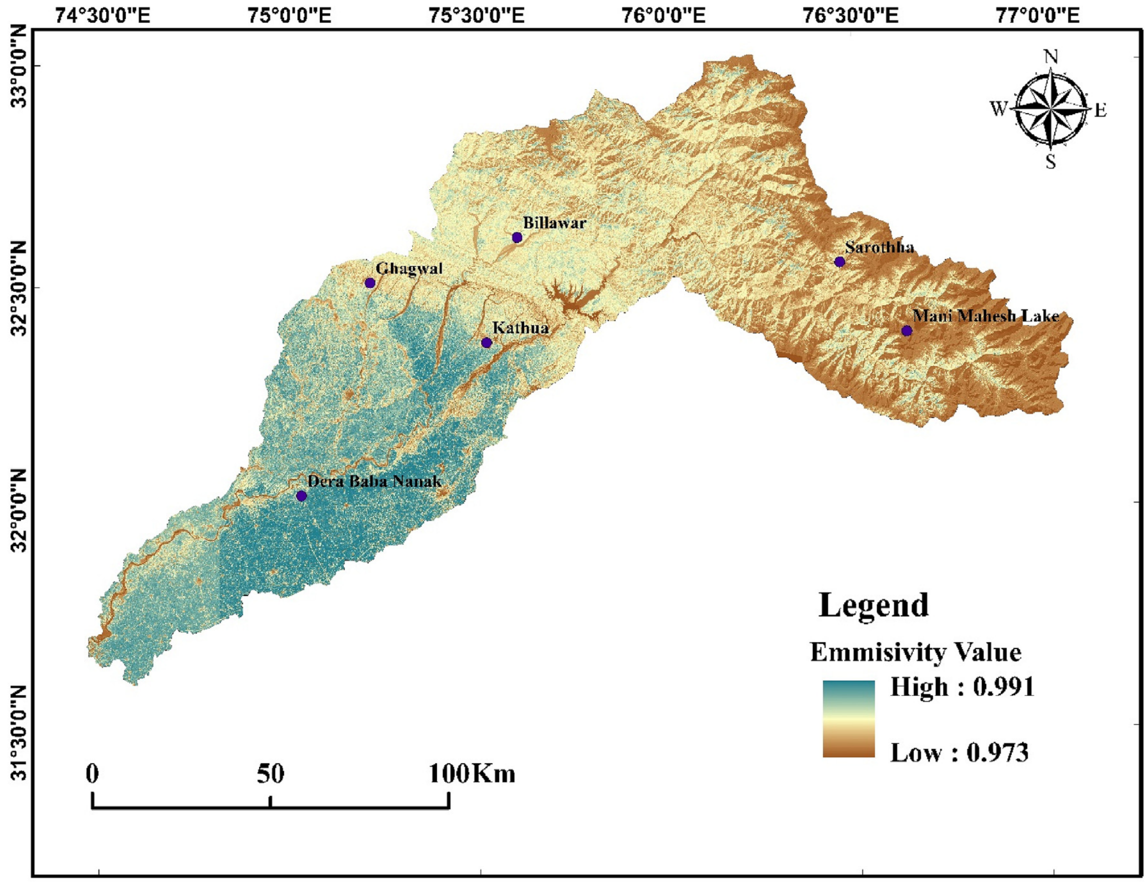

Fig. 6. Land surface emissivity map of the study area.

LTS = land surface temperature,
K1 and K2 = Calibration constants (Table 3 as derived from metadata file), and
LS = Surface radiance.

The LST is the radiative skin temperature of the land surface, as measured in the direction of the remote sensor. It is estimated from ToA brightness temperatures from the infrared spectral channels of a constellation of geostationary satellites. Its estimation further depends on the albedo, the vegetation covers and the soil moisture.

LST is a mixture of vegetation and bare soil temperatures. Because both respond rapidly to changes in the incoming solar radiation due to cloud cover, aerosol load modifications and diurnal variation of illumination, the LST displays quick variations too. In turn, the LST influences the partition of energy between ground and vegetation, and determines the surface air temperature. This is effectively, the earth's surface temperature, as it is directly in contact with the measuring instrument (usually measured in kelvin).

3.8. Calculation of the normalized difference moisture index (NDMI)

The NDMI describes the crop's water stress level and is calculated as the ratio between the difference and the sum of the refracted radiations in the NIR and SWIR regions. The interpretation of the absolute value of the NDMI makes it possible to immediately recognize the areas of farm or field with water stress problems. NDMI is easy to interpret: its values vary between −1 and 1, and each value corresponds to a different agronomic situation, independently of the crop. NDMI was calculated by using equation (8) (Gao, 1996).

$$NDMI = \frac{(NIR - SWIR\ 1)}{(NIR + SWIR\ 1)} \tag{8}$$

3.9. Calculation of normalized difference water index (NDWI)

The NDWI is most the appropriate index for water body mapping. Water bodies have strong absorbability and low radiation in the range from visible to infrared wavelengths. The index uses the green and NIR bands of the remote sensing images based on this phenomenon. The NDWI can enhance the water information effectively in most of the cases. It is sensitive to built-up land and often results in over-estimated water bodies.

NDWI was calculated as follows using equation (9) (McFeeters, 1996):

$$NDWI = \frac{(Green - NIR)}{(Green + NIR)} \tag{9}$$

4. Results and discussion

4.1. Derivation of NDVI

NDVI is a measure of the amount of vegetation at the surface and is related to the health of the vegetation, as healthy vegetation reflects a high amount of energy as compared to the unhealthy and sparse vegetation. The NDVI value of the pixels varies between −1 and +1. Higher values of NDVI indicate rich and healthier vegetation while the lower values indicate poor and sparse vegetation. The NDVI value in the study area varies from 0.509 to −0.106 (Fig. 5). The study shows that northern mountainous, hilly, and rugged terrain have low NDVI value because of

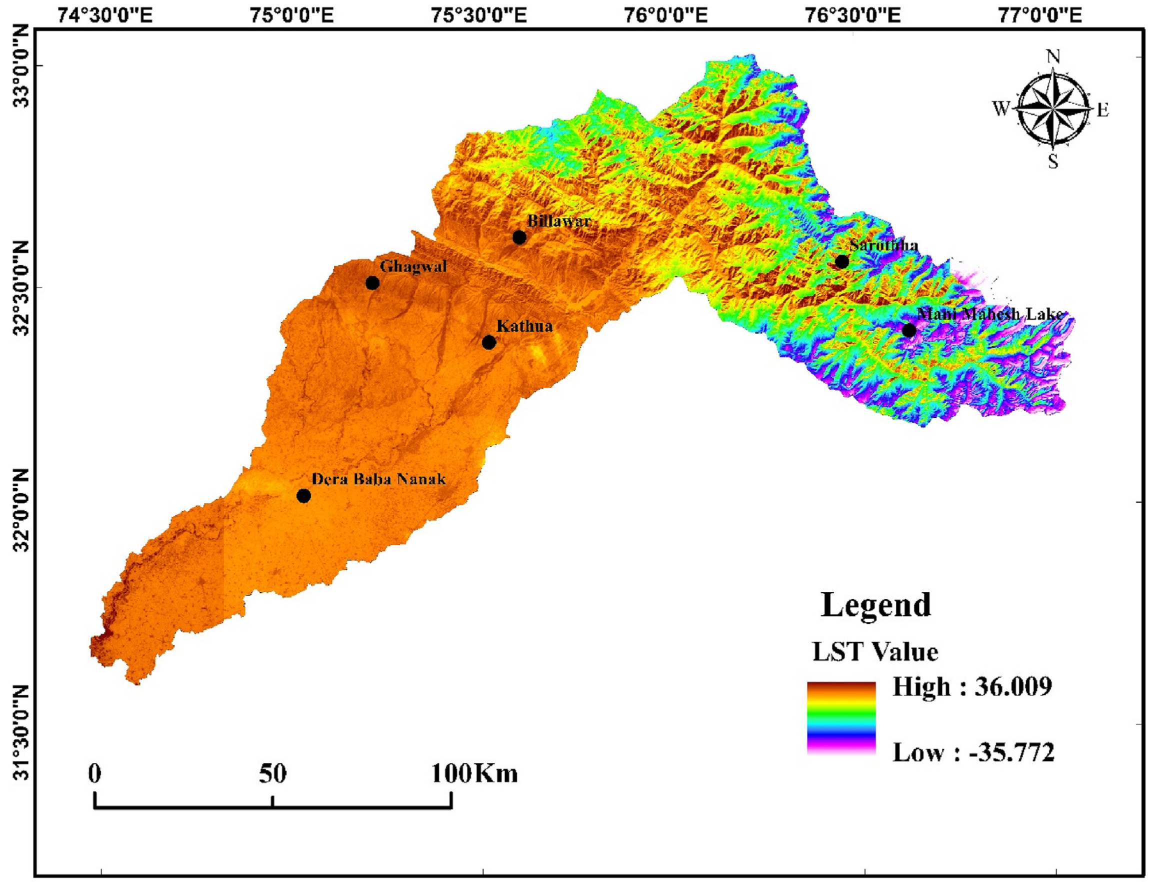

Fig. 7. LST map of the study area.

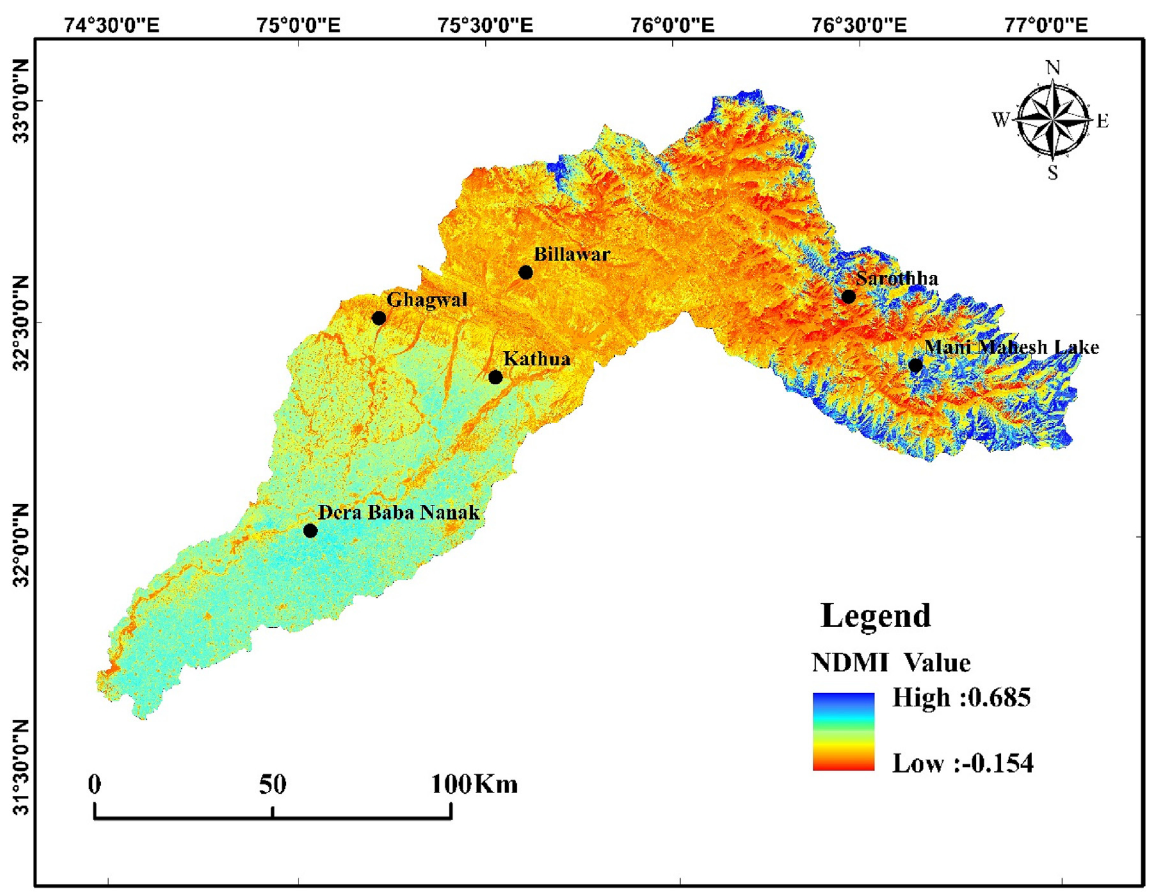

Fig. 8. NDMI map of the study area.

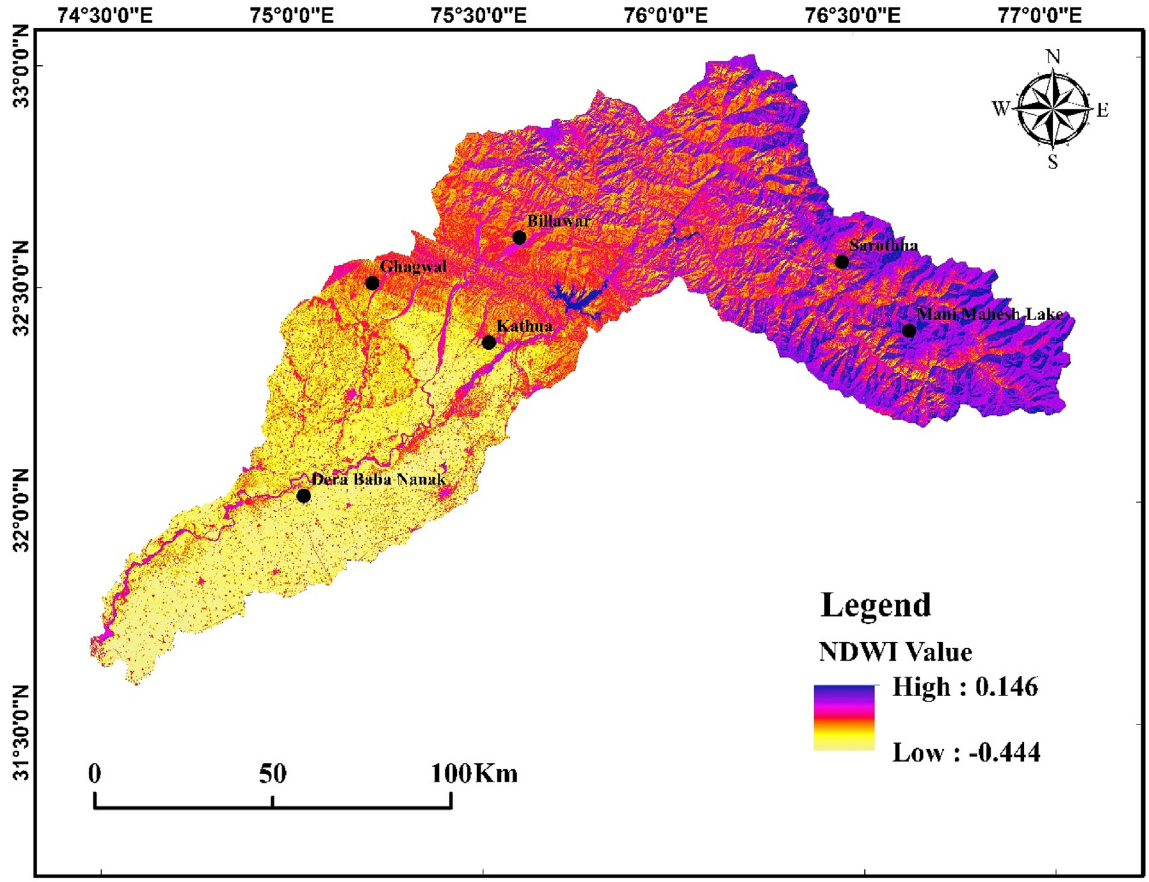

Fig. 9. NDWI map of the study area.

the barren land and glaciers, whereas the southern area includes more agricultural land and shows the high NDVI values.

4.2. Derivation of emissivity

The emissivity of the surface of a material is its effectiveness in emitting energy as thermal radiation, a kind proportionality factor that scales blackbody radiance to predict emitted radiance. It is determined by soil structure, soil composition, organic matter, moisture content, and vegetation-cover characteristics (Van De Griend and Owe, 1993; Jin and Liang, 2006; Malik and Shukla et al., 2018), but does not depend on soil temperature profile or surface temperature. In the present study, the value of the emissivity ranges from 0.991 to 0973 (Fig. 6). It has been observed in the study area that emissivity in forest and other vegetative areas decreases because of a decrease in surface temperature due to an inverse relationship between the LSE and LST. Furthermore, the fractional vegetation cover (FVC) of the study area is estimated, and found to be 0.17 to 0.95.

4.3. Derivation of LST

LST represents the temperature of an object within a pixel, which may include several land cover types. LST maps are prepared to show the spatial distribution of LST within the study area. The maximum LST was observed as 36.009 °C and the minimum LST was observed as −35.0772 °C in January and February (Fig. 7). The results also show that there are variations in the LST of the area due to variations in the topography of the study area. Also shown variations in the snow cover area as well as in barren land and water body coverage. The snow cover areas show temperature well below 0C: we recorded the temperature of Mani Mahesh lake as −35 °C on 26-01-2018 at 10.44 a.m. (local standard time) whereas the satellite data-based result shows that the pixels covering the same area have a temperature of −35.772 °C.

4.4. Derivation of NDMI

The results of the NDMI calculation range from 0.685 to −0.154. It can be seen from the resultant map (Fig. 8) that the high altitude snow covered area is present and the water body locations shows high content of moisture as compared to the plains and low altitude areas. The barren land shows the lowest content of moisture, as there is no presence of vegetation and water bodies. The variations in the NDMI values can be seen in Fig. 7.

4.5. Derivation of NDWI

The NDWI was calculated for observing the water index and it ranges from 0.146 to - 0.444. The areas where water bodies and rivers are present show high values of NDWI as compared to the areas where water bodies/rivers are not present. In the present study, the high altitude areas have a higher value of water index than the agricultural and built up areas, which are generally located in the plains. The high altitude areas also show high moisture content because of the presence of snow cover, whereas the built-up areas show a moderate value of water index due to the presence of water bodies like wells and sewage canals (Fig. 9).

5. Validation of LST

We used Landsat-8 data from January and February in six different strips to determine the LST (Table 2). These satellite based LST results were validated by six field observations on the same date and time as the satellite overpass over the study area, two in HP three in JK, and one

Table 4
In-situ temperature and satellite based LST of the various locations in study area.

S.No.	Location	In-situ Temperature (°C)	Satellite based LST of location(°C)
1	Sarothha (HP	- 28	−29
2	Mani Mahesh Lake (HP	−31	−32
3	Billawar (JK)	17	18
4	Kathua (JK)	16	18
5	Gaghwal (JK)	30	33
6	Dera Baba Nanak (Pb)	21	23

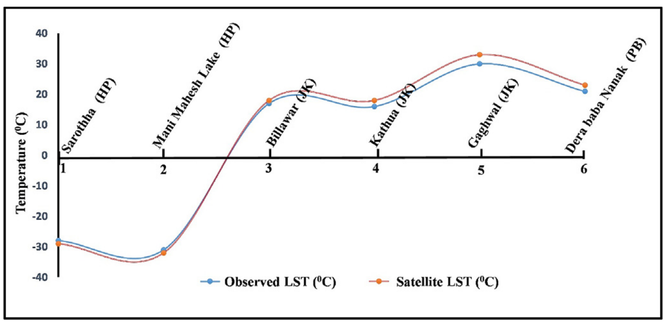

Fig. 10. Relationship between satellite data derived LST & in-situ observed LST.

location in PB, at the local standard time of (10:44 a.m.). The in-situ observations were taken manually with the help of a hand-held thermometer at six locations randomly selected in the study area. The results (Table 4) show that satellite derived LST and in-situ observed LST have a similar pattern and excellent correlation (Fig. 10), which further validates our results.

6. Conclusion

- A model created in ERDAS Imagine 2015 successfully estimated LST using Lansat-8 data in the Ravi basin. The algorithm was created using the brightness temperature of TIRS band 10 and the emissivity of different land covers types, derived from the visible and NIR bands of Landsat 8.
- The retrieved satellite LST was effectively validated with *in-situ observations.*
- The application of robust geospatial technology with freely available data such as Landsat has potential to be effective in monitoring urban growth patterns, hot spot detection, and spatial-temporal climatic changes.
- The effective use of this technology for determining the normalized difference water index, urban index, moisture index, drought index, and vegetation index has immensely enhanced the capability of human beings to further explore remote sensing data for quick and accurate results.
- It is quite hoped that our study will be very helpful to climatologists, environmentalists, and hydrologists in further studies as well as in sustainable planning and management of various natural resources.

Declaration of competing interest

The authors declare that they have no known competing financial interests or personal relationships that could have appeared to influence the work reported in this paper.

Acknowledgments

The authors are highly thankful to the Head, Department of Remote Sensing and GIS, University of Jammu, Jammu for providing the necessary facilities to carry out this work. We are also thankful to the anonymous reviewers for thought provoking comments to improve the quality of the manuscript.

References

Ahmed, B., Kamruzzaman, M., Zhu, X., Rahman, M., Choi, K., 2013. Simulating land cover changes and their impacts on land surface temperature in Dhaka, Bangladesh. Rem. Sens. 5 (11), 5969–5998.
Alam, A., Bhat, M.S., Kotlia, B.S., Ahmad, B., Ahmad, S., Taloor, A.K., Ahmad, H.F., 2017. Coexistent pre-existing extensional and subsequent compressional tectonic deformation in the Kashmir basin, NW Himalaya. Quat. Int. 444, 201–208.
Alam, A., Bhat, M.S., Kotlia, B.S., Ahmad, B., Ahmad, S., Taloor, A.K., Ahmad, H.F., 2018. Hybrid tectonic character of the Kashmir basin: response to comment on "Coexistent pre-existing extensional and subsequent compressional tectonic deformation in the Kashmir basin, NW Himalaya (Alam et al., 2017)" by Shah (2017). Quat. Int. 468, 284–289.
Alexander, C., 2020. Normalised difference spectral indices and urban land cover as indicators of land surface temperature (LST). Int. J. Appl. Earth Obs. Geoinf. 86, 102013.
Arnfield, A.J., 2003. Two decades of urban climate research: a review of turbulence, exchanges f energy and water, and the urban heat island. International Journal of Climate 23, 1–26.
Barsi, J.A., Schott, J.R., Hook, S.J., Raqueno, N.G., Markham, B.L., Radocinski, R.G., 2014. Landsat-8 thermal infrared sensor (TIRS) vicarious radiometric calibration. Rem. Sens. 6 (11), 11607–11626.
Bastiaanssen, W.G.M., Menenti, M., Feddes, R.A., Holtslag, A.A.M., 1998. A remote sensing surface energy balance algorithm for land (SEBAL). 1. Formulation. J. Hydrol. 212, 198–212.
Becker, F., 1987. The impact of spectral emissivity on the measurement of land surface temperature from a satellite. Int. J. Rem. Sens. 8 (10), 1509–1522.
Chand, P., Sharma, M.C., 2015. Glacier changes in the Ravi basin, North-Western Himalaya (India) during the last four decades (1971–2010/13). Global Planet. Change 135, 133–147.
Chand, P., Sharma, M.C., Baruah, U.D., Deswal, S., Latief, S.U., Saini, R., Kumar, P., Prakash, S., Kumar, P., 2019. Shrinking glaciers of the himachal himalaya: a critical review. In: Saikia, A., Thapa, P. (Eds.), Environmental Change in the Himalayan Region. Springer, Cham. https://doi.org/10.1007/978-3-030-03362- 0_5.
Chen, X.L., Zhao, H.M., Li, P.X., Yi, Z.Y., 2006. Remote sensing image-based analysis of the relationship between urban heat island and land use/cover changes. Remote Sens. Environ. (2), 133–146.
Drury, S.A., 1987. Image Interpretation in Geology. Allen and Unwin Publisher Ltd U.K.
Du, C., Ren, H., Qin, Q., Meng, J., Zhao, S., 2015. A practical split-window algorithm for estimating land surface temperature from Landsat 8 data. Rem. Sens. 7 (1), 647–665.
Gao, B.C., 1996. Ndwi - a normalized difference water index for remote sensing of vegetation liquid water from space. Rem. Sens. Environ. 58, 257–266.
Gohain, K.J., Mohammad, P., Goswami, A., 2020. Assessing the Impact of Land Use Land Cover Changes on Land Surface Temperature over Pune City. Quaternary International, India. https://doi.org/10.1016/j.quaint.2020.04.052.
Guo, G., Wu, Z., Xiao, R., Chen, Y., Liu, X., Zhang, X., 2015. Impacts of urban biophysical composition on land surface temperature in urban heat island clusters. Landsc. Urban Plann. 135, 1–10.
Guha, S., Govil, H., Besoya, M., 2020a. An investigation on seasonal variability between LST and NDWI in an urban environment using Landsat satellite data. Geomatics, Nat. Hazards Risk 11 (1), 1319–1345.
Guha, S., Govil, H., Gill, N., Dey, A., 2020b. Analytical study on the relationship between land surface temperature and land use/land cover indices. Spatial Sci. 26 (2), 201–216.
HPSEB, 2004. Chamba Hydro-Electric Project Himachal Pradesh.
Haque, S., Kannaujiya, S., Taloor, A.K., Keshri, D., Bhunia, R.K., Ray, P.K.C., Chauhan, P., 2020. Identification of Groundwater Resource Zone in the Active Tectonic Region of Himalaya through Earth Observatory Techniques. Groundwater for Sustainable Development, p. 100337. https://doi.org/10.1016/j.gsd.2020.100337, 10.
Hulley, G., Veraverbeke, S., Hook, S., 2014. Thermal-based techniques for land cover change detection using a new dynamic MODIS multispectral emissivity product (MOD21). Rem. Sens. Environ. 140, 755–765.
Jiménez-Muñoz, J.C., Cristóbal, J., Sobrino, J.A., Sòria, G., Ninyerola, M., Pons, X., 2008. Revision of the single-channel algorithm for land surface temperature retrieval from Landsat thermal-infrared data. IEEE Trans. Geosci. Rem. Sens. 47 (1), 339–349.
Jin, M., Liang, S., 2006. An improved land surface emissivity parameter for land surface models using global remote sensing observations. J. Clim. 19 (12), 2867–2881.
Joshi, J.P., Bhatt, B., 2012. Estimating temporal land surface temperature using remote sensing: a study of Vadodara urban area, Gujarat. International Journal of Geology, Earth and Environmental Sciences 2 (1), 123–130.
Julien, Y., Sobrino, J.A., 2009. The Yearly Land Cover Dynamics (YLCD) method: an analysis of global vegetation from NDVI and LST parameters. Rem. Sens. Environ. 113 (2), 329–334.
Kalma, J.D., McVicar, T.R., McCabe, M.F., 2008. Estimating land surface evaporation: a review of methods using remotely sensed surface temperature data. Surv. Geophys. 29 (4–5), 421–469.
Kannaujiya, S., Gautam, P.K.R., Chauhan, P., Roy, P.N.S., Pal, S.K., Taloor, A.K., 2020. Contribution of seasonal hydrological loading in the variation of seismicity and geodetic deformation in Garhwal region of Northwest Himalaya. Quat. Int. https://doi.org/10.1016/j.quaint.2020.04.049.

Khan, A., Govil, H., Taloor, A.K., Kumar, G., 2020. Identification of Artificial Groundwater Recharge Sites in Parts of Yamuna River Basin India Based on Remote Sensing and Geographical Information System. Groundwater for Sustainable Development, p. 100415.

Kriegler, F., 1969. Preprocessing transformations and their effects on multispectral recognition. In: Proceedings of the Sixth International Symposium on Remote Sensing of Environment, pp. 97–131.

Kothyari, G.C., Joshi, N., Taloor, A.K., Kandregula, R.S., Kotlia, B.S., Pant, C.C., Singh, R.K., 2019. Landscape evolution and deduction of surface deformation in the Soan Dun, NW Himalaya, India. Quat. Int. 507, 302–323.

Kothyari, G.C., Joshi, N., Thakur, M., Taloor, A.K., Pathak, V., 2020a. Reanalyzing the geomorphic developments along tectonically active Soan Thrust, NW Himalaya, India. Quaternary Science Advances. https://doi.org/10.1016/j.qsa.2020.100017.

Kothyari, G.C., Kandregula, R.S., Chauhan, G., Deasi, B.G., Taloor, A.K., Pathak, V., Swamy, V.K., Mishra, S., Thakkar, M.K., 2020b. Quaternary landform development in the central segment of tectonically active kachchh mainland fault zone, western India. Quaternary Science Advances. https://doi.org/10.1016/j.qsa.2020.100018.

Kothyari, G.C., Pant, P.D., Talukdar, R., Taloor, A.K., Kandregula, R.S., Rawat, S., 2020c. Lateral variations in sedimentation records along the strike length of north almora thrust: central kumaun himalaya. Quaternary Science Advances. https://doi.org/10.1016/j.qsa.2020.100009.

Kour, R., Patel, N., Krishna, A.P., 2016. Influence of shadow on the thermal and optical snow indices and their interrelationship. Rem. Sens. Environ. 187, 119–129.

Kogan, F.N., 2001. Operational space technology for global vegetation assessment. Bull. Am. Meteorol. Soc. (9), 1949–1964.

Kumar, D., Singh, A.K., Taloor, A.K., Singh, D.S., 2020. Recessional pattern of thelu and swetvarn glaciers between 1968 and 2019, bhagirathi basin, garhwal himalaya, India. Quat. Int. https://doi.org/10.1016/j.quaint.2020.05.017.

Lejeune, Q., Davin, E.L., Guillod, B.P., Seneviratne, S.I., 2015. Influence of Amazonian deforestation on the future evolution of regional surface fluxes, circulation, surface temperature and precipitation. Clim. Dynam. 44 (9), 2769–2786.

Liang, X.Z., Xu, M., Yuan, X., Ling, T., Choi, H.I., Zhang, F., Chen, L., Liu, S., Su, S., Qiao, F., He, Y., 2012. Regional climate–weather research and forecasting model. Bull. Am. Meteorol. Soc. 93 (9), 1363–1387.

Malik, M.S., Shukla, J.P., 2018. Retrieving of land surface temperature using thermal remote sensing and GIS techniques in Kandaihimmat watershed, Hoshangabad, Madhya Pradesh. J. Geol. Soc. India 92 (3), 298–304.

Mannstein, H., 1987. Surface energy budget, surface temperature and thermal inertia. In: Remote Sensing Applications in Meteorology and Climatology. Springer, Dordrecht, pp. 391–410.

McFeetemrs, S.K., 1996. The use of the normalized difference water index (NDWI) in the delineation of open water features. Int. J. Rem. Sens. 17, 1425–1432. https://doi.org/10.1080/01431169608948714.

Mustafa, E.K., Co, Y., Liu, G., Kaloop, M.R., Beshr, A.A., Zarzoura, F., Sadek, M., 2020. Study for predicting land surface temperature (LST) using landsat data: a comparison of four algorithms. Adv. Civ. Eng. 2020 https://doi.org/10.1155/2020/7363546.

Norman, J.M., Becker, F., 1995. Terminology in thermal infrared remote sensing of natural surfaces. Agric. For. Meteorol. 77 (3–4), 153–166.

Niclòs, R., Valiente, J.A., Barberà, M.J., Estrela, M.J., Galve, J.M., Caselles, V., 2009. Preliminary results on the retrieval of land surface temperature from MSG- SEVIRI data in Eastern Spain. In: EUMETSAT 2009: Proceedings of Meteorological Satellite Conference, pp. 21–25.

Owen, T.W., Carlson, T.N., Gillies, R.R., 1998. Remotely sensed surface parameters governing urban climate change. Int. J. Rem. Sens. 19, 1663–1681.

Prata, A.J., Caselles, V., Coll, C., Sobrino, J.A., Ottle, C., 1995. Thermal remote sensing of land surface temperature from satellites: current status and future prospects. Rem. Sens. Rev. 12 (3–4), 175–224.

Pareta, K., Pareta, U., 2014. Climate change impact on land and natural resource in Chamba Tehsil of Himachal Pradesh State, India. The International Journal of Science and Technoledge 2 (4), 38–48.

Reddy, S.N., Manikiam, B., 2017. Land surface temperature retrieval from LANDSAT data using emissivity estimation. Int. J. Appl. Eng. Res. 12 (20), 9679–9687.

Sahana, M., Dutta, S., Sajjad, H., 2019. Assessing land transformation and its relation with land surface temperature in Mumbai city, India using geospatial techniques. Int. J. Unity Sci. 23 (2), 205–225.

Sarkar, A., Kumar, V., Jasrotia, A.S., Taloor, A.K., Kumar, R., Sharma, R., Khajuria, V., Raina, G., Kouser, B., Roy, S., 2020a. Spatial analysis and mapping of malaria risk in dehradun city India: a geospatial technology-based decision-making tool for planning and management. In: Geoecology of Landscape Dynamics. Springer, Singapore, pp. 207–221. https://doi.org/10.1007/978-981-15-2097-6_14.

Sarkar, T., Kannaujiya, S., Taloor, A.K., Ray, P.K.C., Chauhan, P., 2020b. Integrated Study of GRACE Data Derived Interannual Groundwater Storage Variability over Water Stressed Indian Regions. Groundwater for Sustainable Development, p. 100376. https://doi.org/10.1016/j.gsd.2020.100376.

Sekertekin, A., Bonafoni, S., 2020. Land surface temperature retrieval from landsat 5, 7, and 8 over rural areas: assessment of different retrieval algorithms and emissivity models and toolbox implementation. Rem. Sens. 12 (2), 294.

Sellers, P.J., Hall, F.G., Asrar, G., Strebel, D.E., Murphy, R.E., 1988. The first ISLSCP field experiment (FIFE). Bull. Am. Meteorol. Soc. 69 (1), 22–27.

Sharma, G., Kannaujiya, S., Gautam, P.R.K., Taloor, A.K., Champatiray, P.K., Mohanty, S., 2020. Crustal deformation analysis across Garhwal Himalaya: Part of western Himalaya using GPS observations. Quat. Int. https://doi.org/10.1016/j.quaint.2020.08.025.

Singh, A.K., Jasrotia, A.S., Taloor, A.K., Kotlia, B.S., Kumar, V., Roy, S., Ray, P.K.C., Singh, K.K., Singh, A.K., Sharma, A.K., 2017. Estimation of quantitative measures of total water storage variation from GRACE and GLDAS-NOAH satellites using geospatial technology. Quat. Int. 444, 191–200.

Singh, S., Sood, V., Taloor, A.K., Prashar, S., Kaur, R., 2020. Qualitative and quantitative analysis of topographically derived CVA algorithms using MODIS and Landsat-8 data over Western Himalayas, India. Quat. Int. https://doi.org/10.1016/j.quaint.2020.04.048.

Sood, V., Gusain, H.S., Gupta, S., Taloor, A.K., Singh, S., 2020a. Detection of snow/ice cover changes using subpixel-based change detection approach over Chhota-Shigri glacier, Western Himalaya, India. Quat. Int. https://doi.org/10.1016/j.quaint.2020.05.016.

Sood, V., Singh, S., Taloor, A.K., Prasher, S., Kaur, R., 2020b. Monitoring and Mapping of Snow Cover Variability Using Topographically Derived NDSI Model over North Indian Himalayas during the Period 2008-19. Applied Computing and Geosciences. https://doi.org/10.1016/j.acags.2020.100040.

Sobrino, J.A., Raissouni, N., 2000. Toward remote sensing methods for land cover dynamic monitoring: application to Morocco. Int. J. Rem. Sens. 21 (2), 353–366.

Taloor, A.K., Joshi, L.M., Kotlia, B.S., Alam, A., Kothyari, G.C., Kandregula, R.S., Singh, A.K., Dumka, R.K., 2020a. Tectonic imprints of landscape evolution in the Bhilangana and Mandakini basin, Garhwal Himalaya, India: a geospatial approach. Quat. Int. https://doi.org/10.1016/j.quaint.2020.07.021.

Taloor, A.K., Kotlia, B.S., Jasrotia, A.S., Kumar, A., Alam, A., Ali, S., Kouser, B., Garg, P.K., Kumar, R., Singh, A.K., Singh, B., 2019. Tectono-climatic influence on landscape changes in the glaciated Durung Drung basin, Zanskar Himalaya, India: a geospatial approach. Quat. Int. 507, 262–273.

Taloor, A.K., Kumar, V., Singh, V.K., Singh, A.K., Kale, R.V., Sharma, R., Khajuria, V., Raina, 'G., Kouser, B., Chowdhary, N.H., 2020b. Land use land cover dynamics using remote sensing and GIS techniques in Western Doon Valley, Uttarakhand, India. In: Geoecology of Landscape Dynamics. Springer, Singapore, pp. 37–51.

Taloor, A.K., Ray, P.K.C., Jasrotia, A.S., Kotlia, B.S., Alam, A., Kumar, S.G., Kumar, R., Kumar, V., Roy, S., 2017. Active tectonic deformation along reactivated faults in Binta basin in Kumaun Himalaya of north India: inferences from tectono-geomorphic valuation. Z. Geomorphol. 61 (2), 159–180.

Taloor, A.K., Pir, R.A., Adimalla, N., Ali, S., Manhas, D.S., Roy, S., Singh, A.K., 2020c. Spring Water Quality and Discharge Assessment in the Basantar Watershed of Jammu Himalaya Using Geographic Information System (GIS) and Water Quality Index(WQI). Groundwater for Sustainable Development. https://doi.org/10.1016/j.gsd.2020.100364.

Tomlinson, C.J., Chapman, L., Thornes, J.E., Baker, C., 2011. Remote sensing land surface temperature for meteorology and climatology: a review. Meteorol. Appl. 18 (3), 296–306.

Van De Griend, A.A., Owe, M., 1993. On the relationship between thermal emissivity and the normalized difference vegetation index for nature surfaces. Int. J. Rem. Sens. 14, 1119–1131.

van Leeuwen, T.T., Frank, A.J., Jin, Y., Smyth, P., Goulden, M.L., van der Werf, G.R., Randerson, J.T., 2011. Optimal use of land surface temperature data to detect changes in tropical forest cover. J. Geophys. Res.: Biogeosciences 116 (G2).

Voogt, J.A., Oke, T.R., 2003. Thermal remote sensing of urban climates. Rem. Sens. Environ. 86 (3), 370–384.

Wanderley, L.N., Domingues, L.M., Joly, C.A., da Rocha, H.R., 2019. Relationship between land surface temperature and fraction of anthropized area in the Atlantic forest region, Brazil. PloS One 14 (12), e0225443.

Wen, L.J., 2017. An analysis of land surface temperature (LST) and its influencing factors in summer in western Sichuan Plateau: a case study of Xichang City. Remote Sensing for Land and Resources 29, 207–214.

Weng, Q., 2009. Thermal infrared remote sensing for urban climate and environmental studies: methods, applications, and trends. ISPRS J. Photogrammetry Remote Sens. 64, 335–344.

Weng, Q., Lu, D., Schubring, J., 2004. Estimation of land surface temperature–vegetation abundance relationship for urban heat island studies. Rem. Sens. Environ. 89 (4), 467–483.

Yao, R., Wang, L., Huang, X., Zhang, W., Li, J., Niu, Z., 2018. Interannual variations in surface urban heat island intensity and associated drivers in China. J. Environ. Manag. 222, 86–94. https://doi.org/10.1016/j.jenvman.2018.05.024.

Yan, Y., Mao, K., Shi, J., Piao, S., Shen, X., Dozier, J., Liu, Y., Ren, H.L., Bao, Q., 2020. Driving forces of land surface temperature anomalous changes in North America in 2002– 2018. Sci. Rep. 10 (1), 1–13. https://doi.org/10.1038/s41598-020-63701-5.

Yu, X., Guo, X., Wu, Z., 2014. Land surface temperature retrieval from Landsat 8 TIRS—comparison between radiative transfer equation-based method, split window algorithm and single channel method. Rem. Sens. 6 (10), 9829–9852.

Yuan, X., Wang, W., Cui, J., Meng, F., Kurban, A., De Maeyer, P., 2017. Vegetation changes and land surface feedbacks drive shifts in local temperatures over Central Asia. Sci. Rep. 7 (1), 3287.